Manipulating the Power of an Additional Phase: A Flower-like Au−Fe$_3$O$_4$ Optical Nanosensor for Imaging Protease Expressions *In vivo*

Jin Xie,[†] Fan Zhang,[†] Maria Aronova,[‡] Lei Zhu,[†] Xin Lin,[†] Qimeng Quan,[†] Gang Liu,[†] Guofeng Zhang,[§] Ki-Young Choi,[⊥] Kwangmeyung Kim,[⊥] Xiaolian Sun,[‖] Seulki Lee,[†,*] Shouheng Sun,[‖] Richard Leapman,[‡] and Xiaoyuan Chen[†,*]

[†]Laboratory of Molecular Imaging and Nanomedicine (LOMIN), National Institute of Biomedical Imaging and Bioengineering (NIBIB), National Institutes of Health (NIH), Bethesda, Maryland 20892, United States, [‡]Laboratory of Cellular Imaging and Macromolecular Biophysics, NIBIB, NIH, Bethesda, Maryland 20892, United States, [§]Biomedical Engineering and Physical Science Shared Resource, NIBIB, NIH, Bethesda, Maryland 20892, United States, [⊥]Biomedical Research Center, Korea Institute of Science and Technology, Seoul 136-791, Korea,, and [‖]Department of Chemistry, Brown University, Providence, Rhode Island 02912, United States

The performance of nanoparticle-based imaging and therapeutic agents depends critically on the properties of the nanoparticle surfaces that interact with the biological milieu and on which the functional grafts are bound. Although it is now possible to overcome the difficulty of synthesizing nanoparticles with a high degree of monodispersity,[1,2] the delicate engineering of the nanoparticle surface that is required to improve the clinical efficacy of nanomaterials remains a challenge.[3,4] In this regard there is a growing need to impart more than one kind of motif onto a single nanoparticle surface to produce a multifunctional agent.[4] Despite a well-developed surface chemistry for a wide range of nanoparticles,[3−7] traditional techniques appear insufficient to produce nanoparticles with the required functionality.

We and others have recently proposed the synthesis of composite nanoparticles that offer strongly enhanced functionality.[8−11] Such particles are constructed from two (or more) discrepant nanocomponents, which exhibit a rich variety of structures and are architecturally intricate, including configurations with dumbbell-,[9,10,12] peanut-,[13] or flower-like shapes.[9] Such composite nanostructures can have considerable advantages, as they introduce a second type of metal surface and thereby multiply the combinations of parameters available for flexibility in design. For example, composite nanoparticles can be loaded with multiple types of motifs.[8,12,14] However, compositeness alone does not fully exploit the potential of such nanostructures. A composite nanoparticle can be viewed as providing a continuous range of separations between two surface types, rather than simply being a conjunction of nanoparticles. Selection of a favorable geometric configuration of the nanoparticle components is needed to yield a composite with the desired functionality. Such an approach has not yet been reported.

ABSTRACT We and others have recently proposed the synthesis of composite nanoparticles that offer strongly enhanced functionality. Here we have used a flower-shaped Au−Fe$_3$O$_4$ nanoparticle as a template to construct an optical probe containing Cy5.5-GPLGVRG-TDOPA on the iron oxide surface and SH-PEG$_{5000}$ on the gold surface that can be specifically activated by matrix metalloproteinases expressed in tumors. Gold nanoparticles have excellent quenching properties, but labile surface chemistry *in vivo*; on the other hand, iron oxide nanoparticles afford robust surface chemistry, but are suboptimal as energy receptors. By a marriage of the two, we have produced a unified structure with performance that is unachievable with the separate components. Our results are a further demonstration that the architecture of nanoparticles can be modulated to tailor their function as molecular imaging/therapeutic agents.

KEYWORDS: composite nanoparticles · Au−Fe$_3$O$_4$ · matrix metalloproteinase · activatable probes · near-infrared fluorescence imaging

RESULTS AND DISCUSSION

Here, we describe the construction of a composite nanoparticle-based activatable probe that can be injected systemically into mice to sense matrix metalloproteinase (MMP) expression *in vivo*. The choice of this experiment stemmed from our previous experience with building activatable probes using gold nanoparticles (GNPs) as templates.[15] GNPs can efficiently absorb energy emitted from an adjacent
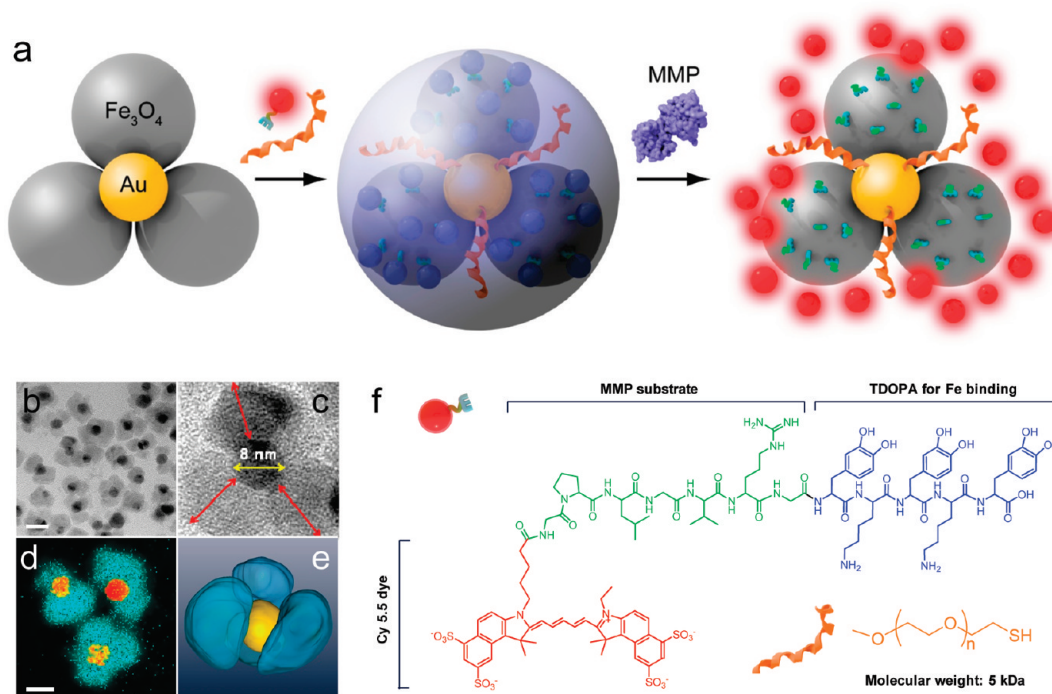
Figure 1. (a) Schematic illustration of the formation and working mechanism of FANPs. (b) High-resolution TEM of the flower-like Au−Fe₃O₄ nanoparticles. Scale bar = 20 nm. (c) Enlarged TEM image of a representative flower-like Au−Fe₃O₄ nanoparticle. The diameter of the GNP core is about 8 nm. The longest distance between the IONP surface and the GNP surface, labeled as red arrows, is 9.7 ± 1.4 nm. (d) Iron map (blue green) superpositioned with the gold cores (yellow-orange) obtained with an electron microscope in the EFTEM mode. (e) Surface-rendered tomogram of a nanoparticle, where false coloring is based on the elemental mapping in (d). (f) Chemical structures of Cy5.5-GPLGVRG-TDOPA and SH-PEG₅₀₀₀.

fluorophore and induce a fluorescently quenched state to the overall nanostructure.[16] The unique surface energy transfer (SET) properties of GNPs allow them to offer larger valid fluorescence quenching distances (∼20 nm) than those of traditional fluorescence resonance energy transfer (FRET). For example, this feature has been harnessed to construct a protease-sensitive probe by using a protease substrate as the spacer to bridge the GNP and the fluorophores. Such probes are of potential clinical relevance in assessing diseases with up-regulation of proteases, such as MMPs, in cancer.[17] The feasibility and superiority of such an approach has been demonstrated by us and others.[15,16,18] The success, however, was mainly achieved *in vitro*, with *in vivo* applications hampered by the unfavorable thiol−gold chemistry, which tends to be labile in a thiol-rich environment such as blood.[19,20] When injected intravenously, gold-based activatable nanoparticles (GANPs) may encounter substantial off-target activation, which jeopardizes the role of GANPs as site-specific probes. There have been efforts to utilize multithiol anchors to improve the stability of the complexation, but with limited success.[21,22]

Our strategy is to replace GNP with a flower-shaped, Au−Fe₃O₄ composite nanoparticle. We expect that with the additional iron oxide surface we can steer clear of gold−thiol chemistry, while still keeping

fluorophores in close vicinity to GNPs, resulting in probes that can be activated in areas of interest after systemic administration. The nanoparticle design is illustrated schematically in Figure 1a. We have chosen GPLGVRG, a sequence with MMP selectivity (such as MMP-2, -9 and -13), as the bridging substrate to be coupled with Cy5.5, a widely used near-infrared dye molecule. On the other end of the peptide we covalently linked an anchoring unit, TDOPA (tridihydroxyphenylalanine, Figure 2). We and other researchers confirmed in previous studies that dopamine and its analogues can bind with high affinity to the surface of iron oxide nanoparticles (IONPs).[23−25] TDOPA is essentially a modified version of such an anchor with improved affinity.[26] In parallel, we applied a thiolated poly(ethylene glycol) (SH-PEG₅₀₀₀) to passivate the gold surface. This measure aims to improve the physiological stability of the overall nanoconjugates and protect the gold surface from cross-tethering by Cy5.5-GPLGVRG-TDOPA. Although first reported by us in 2005,[9] flower-like Au−Fe₃O₄ nanoparticles have not yet been investigated in the context of nanomedicine. We chose a flower shape, rather than dumbbell-shaped structure, because a flower shape bears a multitude of iron oxide "petals" on each GNP core, an architecture that favors accommodation of more ligands in the vicinity of the GNPs, thereby maximizing the use of GNP as a quenching unit.
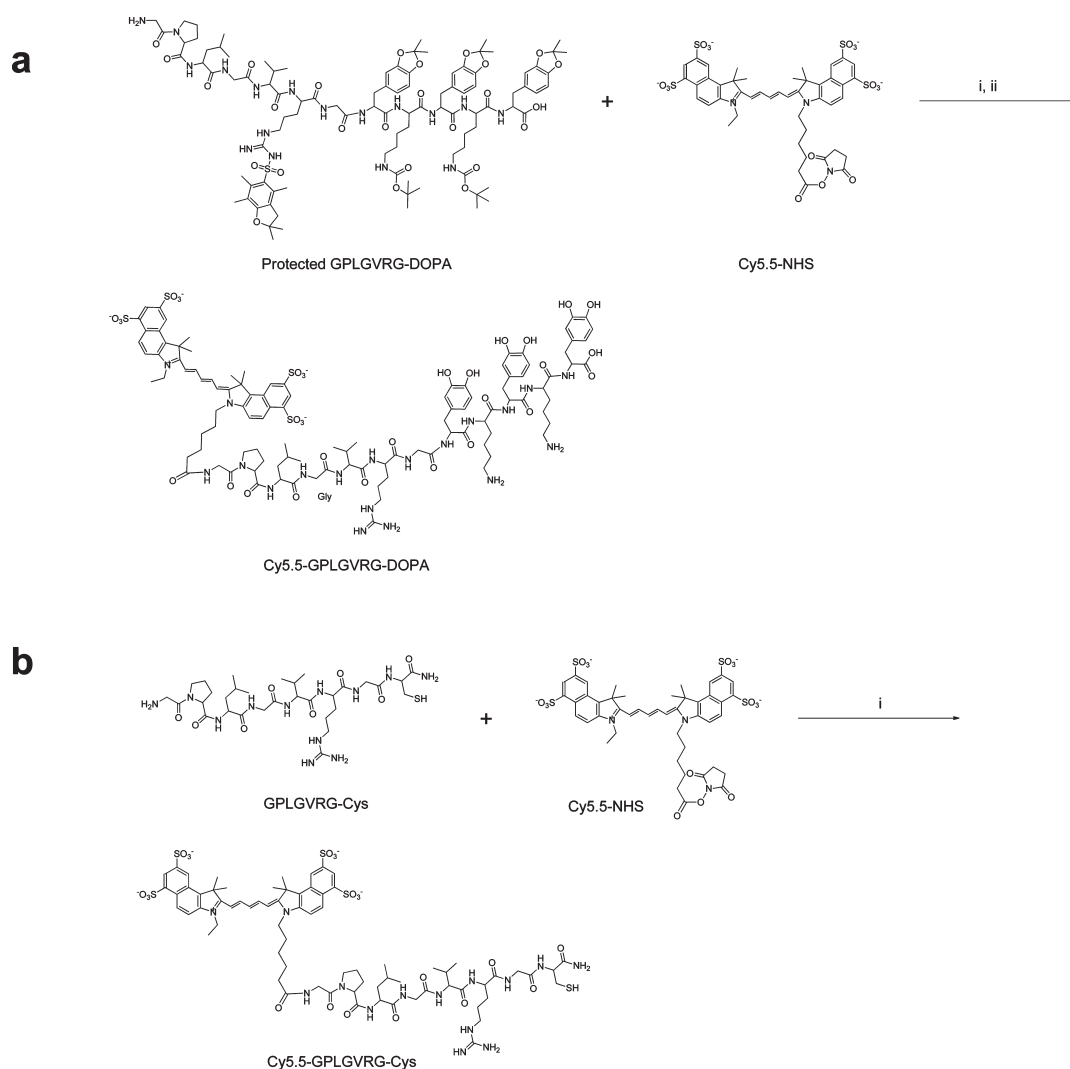
a

Protected GPLGVRG-DOPA   Cy5.5-NHS   i, ii →

Cy5.5-GPLGVRG-DOPA

b

GPLGVRG-Cys   Cy5.5-NHS   i →

Cy5.5-GPLGVRG-Cys

Figure 2. Synthesis of (a) Cy5.5-GPLGVRG-TDOPA and (b) Cy5.5-GPLGVRG-Cys: (i) 2% DIPEA/DMF, (ii) TFA/ethanedithiol/thioanisole/water (80/10/5/5/, v/v/v/v/).

The Au−Fe$_3$O$_4$ nanoparticles were synthesized according to a previously published protocol[9] with minor modification. We first prepared 8 nm GNPs by reducing HAuCl$_4$ in tetralin with oleylamine. We then used the GNPs as seeds to grow Fe$_3$O$_4$ onto the GNP surface *via* pyrolysis using iron pentacarbonyl (Fe(CO)$_5$) as the precursor. As shown in Figure 1b, the IONPs, with a diameter of 13.4 ± 3.5 nm, grew as "petals" around the 8 nm GNP cores, which have higher density and appear darker in TEM images. Each flower-like nanoparticle has an average of 2−4 such petals wrapping around the cores (Figure 1b and c). This observation was in accordance with the inductively coupled plasma (ICP) results, which found an estimated 3:1 ratio between the IONP moiety and the GNP moiety (based on the assumption that each GNP has a diameter of 8 nm and each IONP a diameter of 13 nm). It is noticeable that the longest distance between the IONP surface and the GNP surface (labeled as red arrows in Figure 1c) is about 9.7 ± 1.4 nm, which is well within valid distance

for effective quenching. Iron mapping by energy-filtered TEM (Figure 1d) found almost no overlap between iron and gold, indicating that no alloy was formed during the pyrolysis, and the surface engineering can be processed by considering separate GNPs and IONPs.

Since we aimed at functionalizing both types of surfaces, it was important to know the accessibility of ligands to the gold core. From two-dimensional TEM imaging it is impossible to determine the arrangement of the petals around the gold cores; therefore we used electron tomography to acquire many views of the specimen, which enabled us to generate its three-dimensional structure. As shown in Figure 1e, a surface rendered tomogram, the gold core is accessible by the surroundings, even though it is surrounded by IONPs.

These as-synthesized Au−Fe$_3$O$_4$ nanoparticles were coated with a thick layer of oleic acid/oleylamine and, therefore, could not be dispersed in water.[8] To render the particles water-soluble and to impart the functional

motifs, we incubated the Au–Fe$_3$O$_4$ nanoparticles, which were in a 2:1 CHCl$_3$/DMSO mixture, with Cy5.5-GPLGVRG-TDOPA and SH-PEG$_{5000}$ (see the Methods section) at room temperature (rt) overnight. As a comparison, we also incubated Au–Fe$_3$O$_4$ nanoparticles and IONPs (13 nm in diameter, oleic acid/oleylamine coated, from Ocean Nanotech) with Cy5.5-GPLGVRG-TDOPA (but without SH-PEG$_{5000}$), and, moreover, incubated Au–Fe$_3$O$_4$ nanoparticles with Cy5.5-GPLGVRG-Cys. The Cy5.5-GPLGVRG-Cys sequence was gold-philic and was used in our previous studies to prepare GANPs.[15] As discussed above, we anticipated that by replacing cysteine with TDOPA, the peptide could become iron-philic and be immobilized on an IONP surface, instead of a gold surface. As a control, GANPs were also prepared based on the previously published protocol.[15]

After incubation, all the nanoparticles were washed and redispersed in water with sonication. The supernatant from each washing step was combined and stored for subsequent chemical analysis. The Cy5.5-GPLGVRG-TDOPA can be efficiently immobilized on the iron oxide surface of both IONPs and Au–Fe$_3$O$_4$ nanoparticles (as assessed by the Cy5.5 content in the supernatant). However, the Cy5.5-GPLGVRG-TDOPA, when used alone, failed to convey good water solubility to either the IONPs or Au–Fe$_3$O$_4$ nanoparticles. Cy5.5-GPLGVRG-Cys gave good solubility for GANPs, but not for Au–Fe$_3$O$_4$ nanoparticles. The Au–Fe$_3$O$_4$ nanoparticles incubated with both Cy5.5-GPLGVRG-TDOPA and SH-PEG$_{5000}$, on the other hand, were readily water-soluble after incubation. This suggests the successful immobilization of SH-PEG$_{5000}$ on the gold surface and confirms its critical role as a stabilizing agent. By assessing the content of Cy5.5 in the supernatant, we were able to determine the amount of peptide immobilized onto the nanoparticles, hereafter referred to as flower-like activatable nanoparticles (FANPs). According to the inductively coupled plasma (ICP) results and assuming a diameter of 8 nm for the GNP core in the FANPs, each FANP was estimated to have about 152 ± 12 copies of Cy5.5-GPLGVRG-TDOPA, compared to 85 ± 8 copies per GANP. Since each GANP has a core size of 20 nm, its surface is 6 times greater than that of GNP in the FANPs. Such an increase in peptide loading, despite a loss of gold surface, was attributed to the three petals extending from the gold surface and, once again, suggests that the peptide loading occurred on iron instead of on the gold surface. The overall size of FANPs was 40.0 ± 4.3 nm, as analyzed by dynamic lighter scattering.

As shown in Figure 3a, FANPs have a broad absorption in the visible range (400–800 nm), contributed mainly by the iron oxide moiety. In addition, their spectra exhibit two shoulders at around 560 and 675 nm, which are characteristic absorption bands of GNPs and Cy5.5, respectively. One indicator of the

agglomeration of GNPs is a red-shift of the 560 nm peak.[7] We used such a feature to analyze the stability of FANPs under various conditions, including PBS buffer (137 mM NaCl, 2.7 mM KCl, 10 mM sodium phosphate dibasic, 2 mM potassium phosphate monobasic, pH 7.4), MMP reaction buffer (100 mM Tris, 200 mM NaCl, 5 mM CaCl, 0.1% Brij, pH 7.2), and a concentrated dithiothreitol (DTT) solution (10 mM, in water). Under all these conditions, we observed no aggregation, either visually or spectrometrically, indicating good stability of the FANPs.

The fluorescent activities were measured on an F-7000 fluorescence spectrophotometer (Hitachi). Despite the large amount of Cy5.5-GPLGVRG-TDOPA on the surface, the FANPs showed very low fluorescence activity (Figure 3b, excitation at 675 nm, emission at 690 nm), which was apparently due to the excellent quenching effect of Au–Fe$_3$O$_4$ nanoparticles. Incubating FANPs in PBS or serum (fetal bovine serum, Invitrogen) at 37 °C did not increase the overall fluorescence activity substantially (Figure 3b), suggesting the reliability of the TDOPA–Fe bonding under these conditions. One important criterion of the activatable probes, as we addressed earlier, is their stability against nonspecific activation in a thiol-rich environment. To study this, we incubated FANPs and GANPs at the same Cy5.5 concentration (600 nM) with DTT (a final concentration of 10 mM) and monitored the change of fluorescence over time. We found that under such conditions DTT can almost immediately cleave all the Cy5.5-GPLGVRG-Cys attached to GANPs, but had a minimal impact on FANPs. This observation corresponded well with our expectation that Cy5.5-GPLGVRG was immobilized on the FANPs *via* DOPA–Fe binding and, therefore, was much less liable to thiol cleavage.

After confirming the stability, we then moved forward to test the activation capacity of FANPs by MMP-13. We incubated FANPs with MMP-13 (3 μg/mL) at 37 °C in MMP reaction buffer and measured the fluorescence activities at predetermined time points (Figure 2c). In a control group, we added an MMP inhibitor (MMP inhibitor III, a broad-spectrum inhibitor of various MMPs, EMD Bioscience, 8 μM) in combination with MMP-13 to test whether the activation could be inhibited. Without MMP-13, the FANPs were very stable in the buffer solution, showing almost no signal change within the observation period (420 min). The addition of MMP-13, however, caused a dramatic signal increase, which was efficiently blocked in the control group by the addition of the MMP inhibitor. After 420 min incubation, the activation in signal (between the +MMP-13 group and the –MMP-13 group) was determined to be 17-fold. Such activation was also found to be dependent on MMP-13 concentration. When incubated with MMP-13 at different concentrations (0.2, 0.5, 1, 2, and 4 μg/mL, at 37 °C for 12 h), we observed a
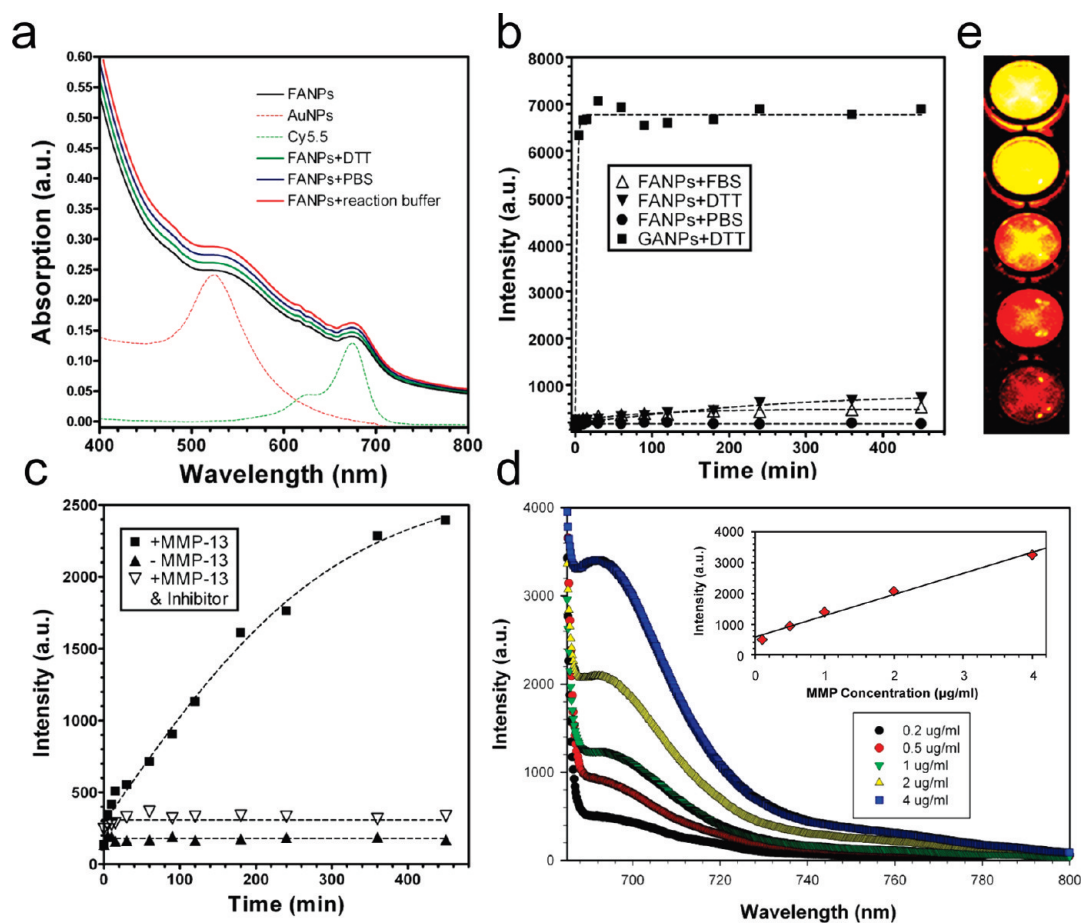
Figure 3. (a) UV−vis spectra of FANPs under various conditions. (b) Stability test of FANPs in PBS, FBS, and DTT. Compared with GANPs, FANPs showed a much better stability than GANPs in a thiol-rich environment. (c) Test of activation capacity by incubating FANPs with MMP-13, with and without the presence of MMP inhibitor. (d) MMP-13 concentration-dependent activation of FANPs. Inset: Activation capacity *vs* MMP-13 concentration. (e) Phantom study with activated FANPs from (d).

proportional increase of fluorescence (Figure 3d). This signal change was visualized better during a phantom study of the activated FANP solution (Figure 3e, on a Maestro 2 imaging system, Cri, Woburn, MA). In general, FANPs showed MMP-specific activation and a much improved stability compared to GANPs. These findings, in conjunction with nontoxicity (Figure 4), make FANP a candidate imaging probe for *in vivo* detection of MMPs.

The *in vivo* tests were performed on an SCC-7 (head and neck squamous cell carcinoma) tumor xenograft model, which is known to express high levels of MMP.[15] Briefly, separate groups of mice received injections by tail vein of either FANPs or GANPs in 200 μL of PBS (150 nmol of Cy5.5/kg), and full-body optical images of the mice were acquired at selected time points (30, 60, 120, and 240 min) postinjection (pi) using an "orange" filter (640−820 nm). In the FANP group the signals were found to be almost exclusively in the tumor area as early as 30 min after the particle injection, and the intensity developed steadily throughout the observation period (Figure 5). By drawing regions of interest (ROIs) around the tumor areas, we were able to assess
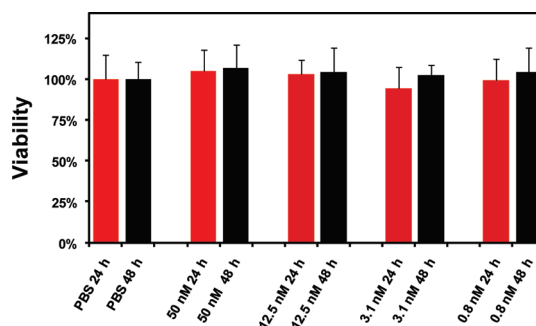

Figure 4. MTT assays with FANPs at different concentrations.

the average signals in the tumor area, which were (414.6 $\pm$ 36.2), (855.4 $\pm$ 134.0), (1164.7 $\pm$ 233.0), and (1523.26 $\pm$ 2.6) $\times$ $10^6 \cdot$phot$\cdot$cm$^{-2}\cdot$s^{-1} at 30, 60, 120, and 240 min pi. For the GANP group, however, the signals were found mostly in the liver at early time points (30, 60, and 120 min), and only at the 240 min pi time point did we observe weak signals from the tumor ((46.8 $\pm$ 13.5) $\times$ $10^6 \cdot$phot$\cdot$cm$^{-2}\cdot$s^{-1} at 240 min). To further confirm that the signals from tumors in the FANP group were indeed induced by MMP cleavage, in
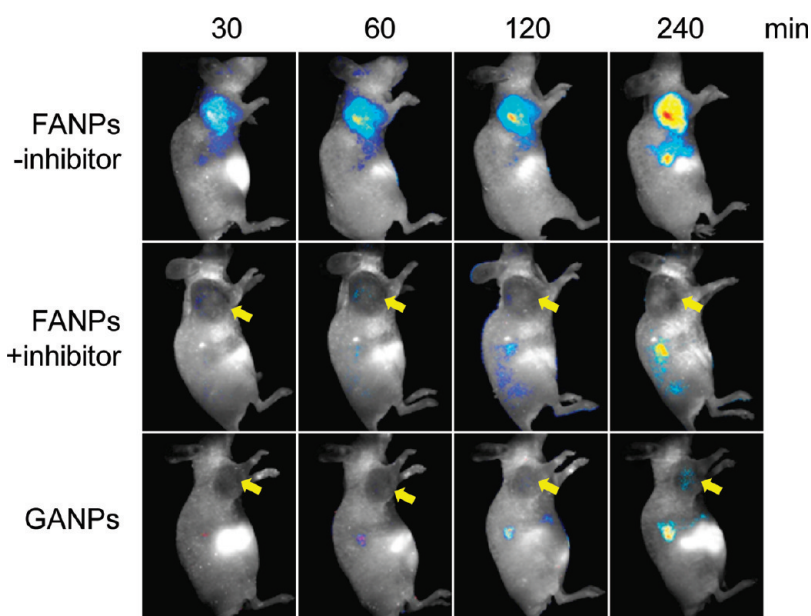
Figure 5. *In vivo* NIRF imaging after the injection of FANPs, with and without the preinjection of MMP inhibitor. In a control group, GANPs at the same Cy5.5 dose were injected.

another control group we injected MMP inhibitor (1 mg/kg) intratumorally into the mice 30 min prior to the FANP injection. The injection of inhibitor induced an almost complete blocking of the FANP activation, as tumor uptake was found to be (26.4 ± 3.1), (31.4 ± 18.7), (27.8 ± 37.5), and $(13.6 \pm 1.4) \times 10^6 \cdot \text{phot} \cdot \text{cm}^{-2} \cdot \text{s}^{-1}$ at 30, 60, 120, and 240 min pi, respectively.

To further elucidate the particle distribution and activation, we sacrificed the mice after imaging at the 4 h time point and collected tumor as well as other major organs for *ex vivo* analysis. We first arranged the organs on a dark plate and subjected them to *ex vivo* imaging on a Meastro 2 optical imaging system. The intensities were then analyzed by the software provided by the vendor (Maestro 2.10.0) and are illustrated as a histogram in Figure 6. Signals from tumors were well correlated with those observed from the *in vivo* imaging, and signals from the FANP group were 10 times more intense than those from the blocking group. The GANPs, on the other hand, showed only a marginal increase in tumor signals compared to the blocking group. Notably, while almost no signals were observed from blood in both FANP groups, we found a strong signal from the blood in the GANP group. This confirmed our previous concern that GANPs may be nonspecifically activated in blood plasma, where glutathione (GSH) is present at high concentration. Besides tumor, the other major intensity-contributing organ was liver, which is not surprising considering the 40 nm diameter of the FANPs. Such a size, together with the antifouling effect afforded by the PEG, also explains the accumulation of FANPs in tumors, which was likely mediated by the enhanced permeability and retention (EPR) effect.[3]

We then performed a series of immunostaining experiments to study FANP distribution and activation in the tissues, for both the MMP blocking and nonblocking groups. We found that the MMP inhibitor did not have a major impact on the tumor accumulation of particles, as manifested by similar Prussian blue staining patterns for tumor tissues in both groups (Figure 7a). As expected, we observed similarly high levels of MMP expression in both tissues, but found almost no Cy5.5 signals in the blocking group. This, together with the Prussian blue results, further confirms our assumption that without active MMPs (the MMP inhibitor does not regulate the MMP expression; rather, it antagonizes and blocks MMP from cleaving the GPLGVRG substrate), the FANPs stayed in an optically well-quenched state in the tumor. On the contrary, we observed strong Cy5.5 signals from the nonblocking group, and their distribution superimposed well with the MMP distribution. This again confirmed our postulation that the activation of FANP probes was specifically mediated by MMPs. Other than in the tumor, we also found significant levels of FANPs in the liver (Figure 7b). This is in accordance with the NIRF results, which showed that liver was a major contributor to the signal. Notably, because FANPs were distributed and activated in the intracellular space, we observed a substantial loss of FANPs by washing, as indicated by both Prussian blue staining and fluorescent immunostaining.

In the current study, by introducing a second iron oxide moiety, we were able to construct an activatable probe that can specifically sense MMP up-regulation *in vivo* after systemic injection. Several factors considered in the design appear to benefit the role of the
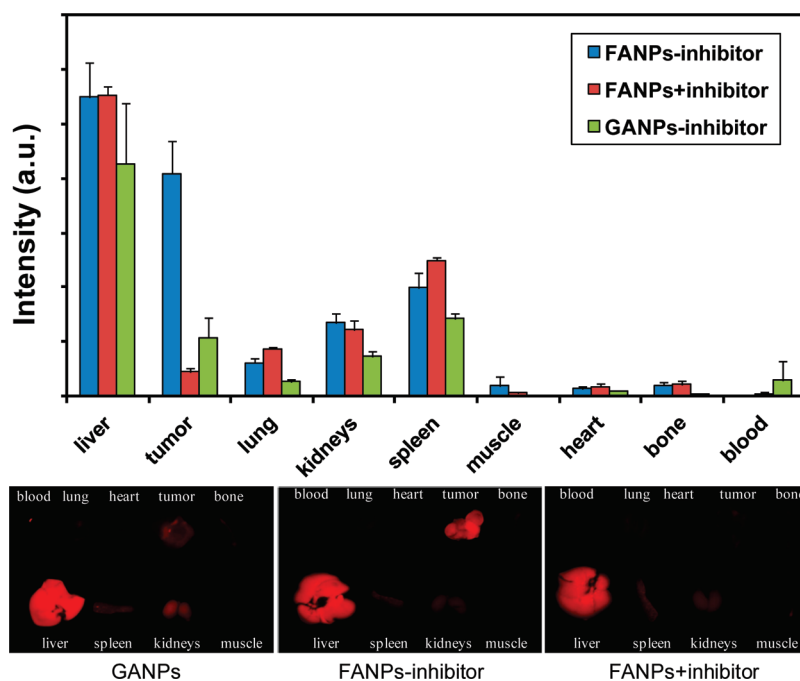
Figure 6. *Ex vivo* imaging of tumor and major organs after the fourth hour of *in vivo* imaging. The intensities from the organs, quantified by the software provided with the Maestro 2 imaging system, are illustrated as histograms in the upper panel.
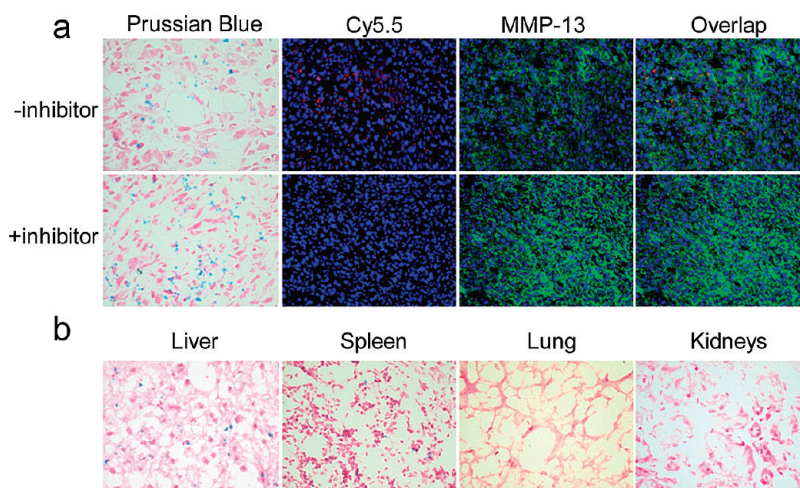

Figure 7. (a) Prussian blue and fluorescent immuostaining results with tumor tissues. While particle distribution and MMP-13 expression were similar, only in the nonblocking group did we observe signals from FANPs. (b) Prussian blue staining of tissues from liver, spleen, lung, and kidneys.

composite nanoconjugate as an efficient probe. First, both GNPs and IONPs are regarded as biologically safe materials and have been separately studied as scaffolds for imaging/therapeutic applications.[3,4,19] Second, although not as effective as GNP, IONPs have been reported to possess an optical quenching effect,[27] which alleviates the possible loss of energy-absorbing ability by moving fluorophores to the iron oxide moiety. Third, the unique flower-like architecture of FANPs allows more fluorophores to be loaded onto a single nanoparticle than with GANPs. This is also an appealing attribute in that each fluorophore on the FANP might in theory be quadruply quenched by (1) its

fluorophore neighbor, (2) the underlying IONP, (3) the other IONPs nearby, and (4) the GNP core. Fourth, although we removed substrates to the IONP surface, this does not mean that the gold surface is not useful. On the contrary, the immobilization of PEG on the gold surface was critical to the stability of the nanoconjugates in a physiological environment. Unlike for GANPs, where Cy5.5-GPLGVRG-Cys is working as the key substrate (and whose unintended detachment disables the particle's ability to serve as an activatable probe), in the FANP system the PEG_{5000}-SH "merely" serves as a stabilizing agent, and such a function seems not to be affected by a thiol-rich environment.

Overall, we have demonstrated that an additional phase incorporated into a composite nanoparticle can be harnessed to optimize the strengths of each nanocomponent. GNPs provide an excellent quenching effect, but have labile surface chemistry in an *in vivo* environment; the IONPs, on the other hand, provide a robust surface conjugation technique, but do not have an appealing quenching effect. By combining the two, we have been able to engineer the surface and thereby integrate the strengths of each. The study has shown a novel way to tailor a material's role in creating imaging/therapeutic agents. It will be interesting to tap further into the potential of such a transition from simple sphere-like GNPs to complex flower-like nanostructures. For example, it should be possible to optimize performance by adjusting the architecture to increase the number of petals in the flower-shaped nanoparticle or to tune the size and shape of each individual component. Moreover, the same technique that was used to target MMP expression in the current study can be readily applied to detect other proteases that are implicated in cancer pathogenesis.

METHODS

Synthesis of Cy5.5-Labeled MMP Substrates. Cy5.5-GPLGVRG-TDOPA (Cy5.5-Gly-Pro-Leu-Val-Arg-Gly-Dopa-Lys-Dopa-Lys-Dopa-OH): The side-chain-protected form of GPLGVRG-TDOPA, Gly-Pro-Leu-Val-Arg(Pbf)-Gly-Dopa(acetonide)-Lys(Boc)-Dopa-(acetonide)-Lys(Boc)-Dopa(acetonide)-OH, was synthesized using standard sold-phase Fmoc peptide chemistry. Cy5.5 succinimide eater (Cy5.5-NHS, 10 mg, 8.86 μmol) was coupled to the N-terminus of protected GPLGVRG-TDOPA (26.7 mg, 13.3 μmol) in anhydrous dimethylformamide (DMF, 2 mL) containing 2% of diisopropylethylamine (DIPEA) at room temperature in the dark. After 2 h the reaction was precipitated in ethyl ether (20 mL), dried *in vacuo*, and purified by semipreparative reversed-phased high-pressure liquid chromatography (RP-HPLC-), yielding 35% to 90% B (A: 0.1% trifluoroacetic acid (TFA) water, B: 0.1% TFA acetonitrile) over 45 min at a flow rate of 10 mL/min. The purified product was deprotected with 2 mL of TFA/ethanedithiol/thioanisole/water (80/10/5/5, v/v/v/v/). After 1 h the reaction was precipitated in ethyl ether, dried *in vacuo*, and further purified by semipreparative RP-HPLC under the same conditions. The purified product was lyophilized and characterized by analytical RP-HPLC and MALDI-TOF. Purity > 95%; mass *m/z* calculated 2338.67, found 2349.2.

Cy5.5-GPLGVRG-Cys (Cy5.5-Gly-Pro-Leu-Val-Arg-Gly-Cys-NH$_2$): Cy5.5-NHS (5 mg, 4.44 μmol) was coupled to the N-terminus of Gly-Pro-Leu-Val-Arg-Gly-Cys-NH$_2$ (5 mg, 6.65 μmol) in anhydrous DMF (1 mL) containing 2% DIPEA at room temperature in the dark. The peptide was further purified and characterized as described above. Purity > 95%; mass *m/z* calculated 1656.96, found 1656.75.

Preparation of Au−Fe$_3$O$_4$ Nanoparticles. Au−Fe$_3$O$_4$ nanoparticles were prepared by following a previously published protocol with minor changes. First, we prepared 8 nm GNPs using HAuCl$_4$·(H$_2$O)$_3$ as the precursor. In brief, 0.2 g of HAuCl$_4$·(H$_2$O)$_3$ was added to 20 mL of tetralin, followed by adding 2 mL of oleylamine. With stirring, a homogeneous solution was formed, which was then heated to 80 °C for 3 h and cooled to room temperature. For purification, ethanol was added, which resulted in the precipitation of GNPs and facilitated their collection by centrifuge. The GNPs were washed again with ethanol and redispersed in 10 mL of hexane. In a second step, 1 mL of oleic acid (3 mmol) was added into 20 mL of octadecene, and the solution was heated at 120 °C for 20 min under Ar protection. Subsequently, 0.3 mL of Fe(CO)$_5$ was injected to the solution, followed by adding 5 mL of 8 nm GNPs in hexane. The solution was heated to 220 °C for 10 min and further refluxed for 20 min. Then, the solution was cooled to room temperature, and the particles were separated and washed with 2-propanol three times. The final product was dispersed in CHCl$_3$.

Preparation of FANPs. In a typical surface modification procedure, 0.4 mg of Cy5.5-GPLGVRG-TDOPA and 25 mg of PEG$_{5000}$-SH in 900 μL of DMSO was added to 2 mL of Au−Fe$_3$O$_4$ (13.75 mg Fe/ml) nanoparticles in CHCl$_3$. The mixture was shaken gently overnight in the dark at room temperature. The particles were then collected by centrifuge, washed with ethanol (2×) and methanol (2×), and then dispersed in water with sonication. The GANPs were prepared by following a previously published protocol.[15]

Elemental Mapping and 3D Rendering. A drop of the solution containing the nanoparticles was deposited and dried on copper grids covered with a Formvar/carbon support film. TEM images of unstained specimens were recorded in the energy filtering mode of the electron microscope (EFTEM) and at a defocus of −2 to −4 μm using a Tecnai TF30 electron microscope (FEI Company) equipped with a GIF Tridiem imaging filter (Gatan Inc.) and operating at an accelerating voltage of 300 kV. To generate the iron map the images were recorded in the EFTEM mode at an energy loss of 683 and 715 eV, in the vicinity of the Fe L2,3 edge with an energy window of 20 eV. The acquisition time for each image was 16 s, and five images for each edge were averaged to increase the signal-to-noise ratio. The Fe signal was calculated by subtracting the background signal at 683 eV from the Fe signal at 715 eV. The calculated signal was smoothed using a median filter and false colored blue-green. To obtain the 3D structure, the particle images were recorded in the TEM mode of the electron microscope, while tilting the specimen through a range of −57° to 69° with 3 degree increments. IMOD software (University of Colorado)[28] was used to generate the tomogram or slices through the volume, which were then segmented and surface rendered using Amira software (Visage Imaging Inc.). The false coloring was done based on the elemental information obtained with EFTEM.

***In Vivo* and *ex Vivo* NIRF Imaging with FANPs and GANPs.** The *in vivo* studies were performed on an SCC-7 (head and neck squamous cell carcinoma) xenograft tumor model. The animal model was prepared by inoculating 1 million SCC-7 cells subcutaneously into the right flanks of mice. The imaging was performed on a Maestro 2 imaging system about one week later, when tumors reached a size of 0.5 cm^3. Both FANPs and GANPs were injected intravenously in 200 μL of PBS at a dose of 150 nmol Cy5.5/kg into different groups of mice. For the control group, MMP inhibitor at a dose of 1 mg/kg was intratumorally injected 30 min prior to the FANP injection. Full-body optical images were acquired at selected time points (30, 60, 120, and 240 min) postinjection using an "orange" filter (640 to 820 nm). The mice were sacrificed after the fourth hour of imaging. Tumor and other major organs were collected and underwent *ex vivo* imaging on the Maestro 2.

Fluorescence Immunostaining: Prussian Blue Staining. After the 4 h scan, the mice were sacrificed and the tumor, liver, spleen, kidney, and lung were collected and kept in optimal cutting temperature compound at −80 °C. Prior to the staining, the tissue blocks were taken out and cut into 4 μm sections. For Prussian blue staining, the tissue slices were incubated in 10% potassium ferrocyanide (Perl's reagent; Sigma) with 20% HCl for 20 min and were then washed and counterstained with

erythrosin. The Fe content was visualized as blue dots after the staining. The tissue slices were incubated with FITC-labeled anti-MMP-9 antibody (Abcam) at a dilution of 1:200 and 1:400, respectively, for MMP-9 and MMP-13 staining. Then images were taken on a fluorescence microscope (excitation filter: 530−585 nm; emission filter: 605−680 nm; Olympus BX61, Olympus America Inc., Melville, NY).

REFERENCES AND NOTES

1. Lee, J. H.; Huh, Y. M.; Jun, Y.; Seo, J.; Jang, J.; Song, H. T.; Kim, S.; Cho, E. J.; Yoon, H. G.; Suh, J. S.; *et al.* Artificially Engineered Magnetic Nanoparticles for Ultra-Sensitive Molecular Imaging. *Nat. Med.* **2007,** *13*, 95–99.

2. Park, J.; Lee, E.; Hwang, N. M.; Kang, M. S.; Kim, S. C.; Hwang, Y.; Park, J. G.; Noh, H. J.; Kini, J. Y.; Park, J. H.; *et al.* One-Nanometer-Scale Size-Controlled Synthesis of Monodisperse Magnetic Iron Oxide Nanoparticles. *Angew. Chem., Int. Ed.* **2005,** *44*, 2872–2877.

3. Xie, J.; Huang, J.; Li, X.; Sun, S.; Chen, X. Iron Oxide Nanoparticle Platform for Biomedical Applications. *Curr. Med. Chem.* **2009,** *16*, 1278–1294.

4. Xie, J.; Lee, S.; Chen, X. Nanoparticle-Based Theranostic Agents. *Adv. Drug Delivery Rev.* **2010,** *62*, 1064–1079.

5. Medintz, I. L.; Uyeda, H. T.; Goldman, E. R.; Mattoussi, H. Quantum Dot Bioconjugates for Imaging, Labelling and Sensing. *Nat. Mater.* **2005,** *4*, 435–446.

6. Sun, C.; Lee, J. S.; Zhang, M. Magnetic Nanoparticles in MR Imaging and Drug Delivery. *Adv. Drug Delivery Rev.* **2008,** *60*, 1252–1265.

7. Rosi, N. L.; Mirkin, C. A. Nanostructures in Biodiagnostics. *Chem. Rev.* **2005,** *105*, 1547–1562.

8. Xu, C.; Xie, J.; Ho, D.; Wang, C.; Kohler, N.; Walsh, E. G.; Morgan, J. R.; Chin, Y. E.; Sun, S. Au-Fe$_3$O$_4$ Dumbbell Nanoparticles As Dual-Functional Probes. *Angew. Chem., Int. Ed.* **2008,** *47*, 173–176.

9. Yu, H.; Chen, M.; Rice, P. M.; Wang, S. X.; White, R. L.; Sun, S. Dumbbell-Like Bifunctional Au-Fe$_3$O$_4$ Nanoparticles. *Nano Lett.* **2005,** *5*, 379–382.

10. Choi, S. H.; Na, H. B.; Park, Y. I.; An, K.; Kwon, S. G.; Jang, Y.; Park, M. H.; Moon, J.; Son, J. S.; Song, I. C.; *et al.* Simple and Generalized Synthesis of Oxide-Metal Heterostructured Nanoparticles and Their Applications in Multimodal Biomedical Probes. *J. Am. Chem. Soc.* **2008,** *130*, 15573–15580.

11. Wang, C.; Xu, C.; Zeng, H.; Sun, S. Recent Progress in Syntheses and Applications of Dumbbell-like Nanoparticles. *Adv. Mater. Deerfield* **2009,** *21*, 3045–3052.

12. Choi, J. S.; Jun, Y. W.; Yeon, S. I.; Kim, H. C.; Shin, J. S.; Cheon, J. Biocompatible Heterostructured Nanoparticles for Multimodal Biological Detection. *J. Am. Chem. Soc.* **2006,** *128*, 15982–15983.

13. Wang, C.; Tian, W.; Ding, Y.; Ma, Y. Q.; Wang, Z. L.; Markovic, N. M.; Stamenkovic, V. R.; Daimon, H.; Sun, S. Rational Synthesis of Heterostructured Nanoparticles with Morphology Control. *J. Am. Chem. Soc.* **2010,** *132*, 6524–6529.

14. Gu, H.; Yang, Z.; Gao, J.; Chang, C. K.; Xu, B. Heterodimers of Nanoparticles: Formation at a Liquid−Liquid Interface and Particle-Specific Surface Modification by Functional Molecules. *J. Am. Chem. Soc.* **2005,** *127*, 34–35.

15. Lee, S.; Cha, E. J.; Park, K.; Lee, S. Y.; Hong, J. K.; Sun, I. C.; Kim, S. Y.; Choi, K.; Kwon, I. C.; Kim, K.; *et al.* A Near-Infrared-Fluorescence-Quenched Gold-Nanoparticle Imaging Probe for In Vivo Drug Screening and Protease Activity

16. Dubertret, B.; Calame, M.; Libchaber, A. J. Single-Mismatch Detection Using Gold-Quenched Fluorescent Oligonucleotides. *Nat. Biotechnol.* **2001,** *19*, 365–370.

17. Turk, B. Targeting Proteases: Successes, Failures and Future Prospects. *Nat. Rev. Drug Discovery* **2006,** *5*, 785–799.

18. Oh, E.; Hong, M. Y.; Lee, D.; Nam, S. H.; Yoon, H. C.; Kim, H. S. Inhibition Assay of Biomolecules Based on Fluorescence Resonance Energy Transfer (FRET) between Quantum Dots and Gold Nanoparticles. *J. Am. Chem. Soc.* **2005,** *127*, 3270–3271.

19. Ghosh, P.; Han, G.; De, M.; Kim, C. K.; Rotello, V. M. Gold Nanoparticles in Delivery Applications. *Adv. Drug Delivery Rev.* **2008,** *60*, 1307–1315.

20. Jones, D. P.; Carlson, J. L.; Samiec, P. S.; Sternberg, P., Jr.; Mody, V. C., Jr.; Reed, R. L.; Brown, L. A. Glutathione Measurement in Human Plasma. Evaluation of Sample Collection, Storage and Derivatization Conditions for Analysis of Dansyl Derivatives by HPLC. *Clin. Chim. Acta* **1998,** *275*, 175–184.

21. Rosi, N. L.; Giljohann, D. A.; Thaxton, C. S.; Lytton-Jean, A. K.; Han, M. S.; Mirkin, C. A. Oligonucleotide-Modified Gold Nanoparticles for Intracellular Gene Regulation. *Science* **2006,** *312*, 1027–1030.

22. Abad, J. M.; Mertens, S. F.; Pita, M.; Fernandez, V. M.; Schiffrin, D. J. Functionalization of Thioctic Acid-Capped Gold Nanoparticles for Specific Immobilization of Histidine-Tagged Proteins. *J. Am. Chem. Soc.* **2005,** *127*, 5689–5694.

23. Xie, J.; Xu, C.; Kohler, N.; Hou, Y.; Sun, S. Controlled PEGylation of Monodisperse Fe$_3$O$_4$ Nanoparticles for Reduced Non-Specific Uptake by Macrophage Cells. *Adv. Mater.* **2007,** *19*, 3648–3652.

24. Xie, J.; Chen, K.; Huang, J.; Lee, S.; Wang, J.; Gao, J.; Li, X.; Chen, X. PET/NIRF/MRI Triple Functional Iron Oxide Nanoparticles. *Biomaterials* **2010,** *31*, 3016–3022.

25. Xu, C.; Xu, K.; Gu, H.; Zheng, R.; Liu, H.; Zhang, X.; Guo, Z.; Xu, B. Dopamine as a Robust Anchor to Immobilize Functional Molecules on the Iron Oxide Shell of Magnetic Nanoparticles. *J. Am. Chem. Soc.* **2004,** *126*, 9938–9939.

26. Statz, A. R.; Meagher, R. J.; Barron, A. E.; Messersmith, P. B. New Peptidomimetic Polymers for Antifouling Surfaces. *J. Am. Chem. Soc.* **2005,** *127*, 7972–7973.

27. Josephson, L.; Kircher, M. F.; Mahmood, U.; Tang, Y.; Weissleder, R. Near-Infrared Fluorescent Nanoparticles as Combined MR/Optical Imaging Probes. *Bioconjugate Chem.* **2002,** *13*, 554–560.

28. Kremer, J. R.; Mastronarde, D. N.; McIntosh, J. R. Computer Visualization of Three-Dimensional Image Data Using IMOD. *J. Struct. Biol.* **1996,** *116*, 71–76.